



Supplementary Material for

Jumping on water: Surface tension–dominated jumping of water striders and robotic insects

Je-Sung Koh, Eunjin Yang, Gwang-Pil Jung, Sun-Pill Jung, Jae Hak Son, Sang-Im Lee, Piotr G. Jablonski, Robert J. Wood, Ho-Young Kim,* Kyu-Jin Cho*

*Corresponding author. E-mail: hyk@snu.ac.kr (H.-Y.K.); kjcho@snu.ac.kr (K.-J.C.)

Published 31 July 2015, *Science* **349**, 517 (2015)
DOI: 10.1126/science.aab1637

This PDF file includes:

Materials and Methods
Supplementary Text
Figs. S1 to S13
Tables S1 to S7

Other Supplementary Material for this manuscript includes the following:
(available at www.sciencemag.org/content/349/6247/517/suppl/DC1)

Movies S1 to S5

Materials and Methods

1. Measurements of and Experiments on Water Striders Jumping Water

Water striders (*Aquarius paludum*) were collected from streams and ponds around the city of Seoul, Korea. Insects were placed individually in a square acrylic bath (70 mm wide) half-filled with water (normal tap water), and their jumping behaviors were recorded from front and side views simultaneously, using two high-speed cameras (TS 1000ME) at 1000 frames per second. Four jumps by four adult water striders were recorded and analyzed. The inclinations of the jump trajectory were between 60° and 80° of the horizontal (two jumps by two males and two jumps by two females; see Table S1 for kinematic parameters). The jumps were induced by touching the insect with a rigid stick positioned below its body; all the analyzed jumps were checked to verify that the jumping motion was not influenced by the stimulating stick. Because we only focused on vertical jumping speed from the water surface, we measured only the vertical component of motion of the insects' legs and bodies from the movies. The animals used in this study were handled in accordance with institutional guidelines for the care and use of laboratory animals.

2. Measurements of and Experiments on the Robot

Velocity and position data were captured by vision analysis software (Proanalyst). The jumping video was recorded by a high-speed camera system (MotionXtraNx3-S3, IDT Ltd., UK) at 3000 frames per second. Seven tracking points were put on the robot structure, and the velocity and position of the virtual center of mass were computed from data collected from these points. Finally, velocity and position were plotted to a millisecond resolution (Figs. S1-S3).

The robot was untethered but triggered by external heat. The heating wire (Ni-Cr wire) protruded 1 mm from the free surface, and the actuator was positioned right above the heating wire when the robot was put on the free surface. The actuator was heated by thermal convection around the heating wire until the torque direction reversed.

3. Fabrication and Materials

The robot structure was designed so that the smart composite microstructures (SCM) manufacturing process could be applied (24). This process facilitates the development of microscale linkage structures by lamination of multiple sheets cut by precision laser machining. In this manufacturing process, the planar folding pattern creates 3D shapes that become the final robot structure after adhesion. The structure is primarily composed of glass fiber reinforced plate (GFRP), which is made by curing five layers of fabric glass prepreg (Realcarbon Co.) in a heat press (140°C, 550 kPa, 1 hr). The GFRP was cut by a UV laser machining system (AWAVE- 355nm-3W-Nd:YVO4-DPSS laser, Advanced Optowave Co.) (Fig. S5).

Supplementary Text

1. Stiffness of the Sheet SMA Actuator

The stiffness of the shape memory alloy (SMA) actuator, k , is increased by increasing the temperature of the actuator. It is difficult to measure and control the

temperature precisely. Reliable actuator stiffness may be calculated by modeling the passive trigger component and the stroke of the actuator. The beam deflection model is employed to obtain the triggering force, and the stroke of the sheet SMA coil actuator can be measured. The force and deflection of the passive trigger is expressed in equation (1), the cantilever deflection model with the width and thickness of the passive trigger as illustrated in Fig. S6 A and B,

$$F \cdot \alpha = 2 \cdot \frac{2EI}{L_t^2} \delta \quad (I = \frac{w\tau^3}{12}) \quad (1)$$

where F is the actuation force, α is the moment arm of the passive trigger, L_t is the length, w is the width of the cantilever, τ is the cantilever thickness, δ is the required deflection for passive triggering, and E is the characteristic modulus of the composite material.

The characteristic modulus of the composite material should be obtained by experiments on specimens with passive triggers of varying widths and thicknesses, to produce varying degrees of stiffness. Experiments were performed on a range of passive trigger specimens to determine the relationship between pulling force and deflection (Fig. S6C). The characteristic modulus of the composite materials was computed to be 0.93 Gpa, and the modeling results with this values matched well with experiments (Fig. S6D). Using the model, we can design the triggering force of the passive trigger when it attains the required deflection for triggering. The required deflection is determined by the initial body angle, θ . The prototypes have the same initial angle of 32° , which corresponds to 0.8 mm of desired deflection. Finally, the stiffness of the actuator, k , can be calculated by dividing the triggering force by actuator stroke:

$$Actuator\ Stiffness(k) = \frac{Triggering\ Force(F)}{Actuator\ Stroke(s)} \quad (2)$$

By varying the design of the passive trigger, various robot prototypes with different actuator stiffnesses were prepared. Table S2 lists their driving forces.

2. Water Surface Modeling for the Real and the Robotic Water Strider

The lifting force in jumping on water is created from various hydrodynamic forces that are in effect between the driving legs and the water surface. During jumping on the ground the reaction force on a rigid surface directly lifts the body. Fig. S7 shows the dynamic parameters for the real and the robotic water strider and the hydrodynamic forces between the leg and the water surface. The drag force due to form drag and skin friction, F_d , is exerted on the moving leg with a certain velocity. The buoyancy, F_b , and the surface tension force, F_s , correspond to the weight of water that would fill the dimple. The added inertia, F_i , arises when the fluid is accelerated by the accelerating leg. Then we may write the total forces as follows (14):

$$F_w \approx \underbrace{C_d \rho r L_s U^2}_{\text{Drag } F_d} + \underbrace{\left(\frac{\pi}{2} \rho g r^2 L_s + 2 \rho g r d L_s \right)}_{\text{Buoyancy } F_b} + \underbrace{\pi \rho r^2 L_s a}_{\text{Added mass } F_i} + \underbrace{2 \sigma L_s}_{\text{Surface tension } F_s} \quad (3)$$

where C_d is the drag coefficient, ρ is the density of water, U is the speed of the leg, L_s is the wetted length of the leg, g is the gravitational acceleration, h is the depth of the

dimple, a is the acceleration of the leg, σ is the surface tension coefficient, and r is the radius of the leg.

On the water surface, driving force is generated by hydrodynamic forces exerted on the driving legs when the legs push down the water surface. The force ratios for water striders and robotic striders with regard to the surface tension force are scaled as $F_d/F_s \sim 10^{-2}$, $F_b/F_s \sim 10^{-2}$, and $F_i/F_s \sim 10^{-3}$. The hydrodynamic forces differ depending on whether the legs break the water surface or not, because the surface tension force—the largest of the hydrodynamic forces—is lost when the surface is broken. Using characteristic values for water strider locomotion, the approximate magnitudes of each term in the hydrodynamic equation (3) were estimated. The characteristic parameters of water strider locomotion listed in Table S4, have been adopted from Vella *et al.* (14).

Table S5 shows the calculated dimensionless numbers to compare the scales of various hydrodynamic forces. Comparing the water strider and the robot, the values are similar, and we can deduce the force exerted by the surface tension of the water is much larger than the other forces. The thin, wire-shaped legs have very small characteristic area and volume, which minimizes form drag, buoyancy, and the added mass effect. The viscous force is small with the velocity of common arthropods on water. Therefore, the surface tension force is the dominant factor in the reaction force of the water jumping arthropods. However, this is true only if the water surface is unbroken. If the legs penetrate the water surface, the surface tension force disappears immediately.

A sudden drop in the supporting force on water drastically decreases the takeoff velocity. In terms of the energy transfer, the momentum of water around the legs increases when the legs break the water surface, and the energy loss to the kinetic energy of water reduces the vertical kinetic energy of the water strider. E_s (the stored energy in the actuator) is transferred into the kinetic energy of the robot ($1/2 mv_b^2$), water kinetic and surface energy, vibration, friction, and so forth.

$$E_s \rightarrow \frac{1}{2}mv_b^2 + \text{water kinetic } E + \text{water surface } E + \text{vibration} + \text{friction loss} + \dots \quad (4)$$

When the water kinetic and surface energy are increased in a constant stored energy, the kinetic energy of the jumping body is reduced.

The surface tension force is the dominant force for locomotion on water (2, 4, 6, 11, 27, 28). In this study, the static calculation is used to estimate the capillary force on the moving leg following a calculation of the Weber number. Vella (14) reported the sinking characteristics of the cylinder impinging on the liquid surface. That study describes the effect of We on sinking dynamics, showing that the maximum deformation of meniscus upon sinking with small We converges to that of a cylinder gently placed on the liquid surface. In addition, the load bearing capacity of a liquid surface with a small Froude number ($F=U/(gl_c)^{1/2}$) does not differ much from the static load bearing capacity.

Vella's study addressed small objects that impinge with initial velocity and are subsequently decelerated by the liquid. In contrast, the legs of real water striders, and of our robot, initially rest on the surface, leading to much smaller acceleration of water in the early stage than in the impinging cylinder case. Although these two motion are not the same, the qualitative tendency toward negligible dynamic effects with small We would still be valid for the leg stroke during water jumping. Since the We of the water striders and our robot, as listed in Table S5, are small enough to assume a surface-tension-

dominant phenomenon with negligible dynamic effects, the interfacial force estimation based on the depth of the meniscus can be applied. As a result, the model yields simulations that are well-matched with our experiments within 7% error in take-off velocity.

We measured the surface tension force around the leg of the robot prototype experimentally. We prepared two leg shapes (round and square) and used a tensile test machine with a precise electronic balance to push the specimens down on the water surface, as shown in Fig. S8. The experiments were performed with raw wire and hydrophobic coated wire in two shapes to determine the effect of hydrophobicity. With the hydrophobic coating, 150° of the contact angle is achieved, whereas the raw SMA wire achieves only 75° , as shown in Fig. S9. Results obtained for the round-shaped leg show a linear relationship between the surface tension force and depth (Fig. S10). The shape of the leg influences the surface tension force because it affects the depth of the wetted legs. Actually, water striders have flexible legs that are held bent when they float and move on water. The surface tension force around a cylinder bent on the water surface has been studied, and it can be computed analytically (14, 29). Based on this research, we can compute the surface tension force around the leg of the robotic water strider.

The surface tension force per unit length, f_s , is shown in the following equation:

$$f_s(h) = 2\rho g l_c \cdot h \sqrt{1 - (h/2l_c)^2} \quad (5)$$

$$l_c = \sqrt{\frac{\sigma}{\rho g}}$$

where ρ is the density of water, g is the gravitational acceleration, h is the depth of the center of the cylinder beneath the free surface of water, and l_c is the capillary length of water. The resulting surface tension force of the leg (F_s) is the integration of the surface tension force per unit length along the wetted length (L_s). This is shown in Fig. S11.

$$F_s(h) = \int f_s(h) dL_s \quad (6)$$

The modeling results and experimental measurements match well, as shown in Fig. S12. For the round-shaped leg, error increases as depth increases. The measured force becomes smaller than the modeling force because the actual contact length is reduced by deformation of the free surface, as shown in Fig. S11. The round-shaped leg shows a more linear relationship between surface tension force and depth, like a linear spring. Therefore, the slope of the graph is assumed to be the stiffness of the water surface. By modeling the water surface as a spring-damper system, dynamic modeling of the robot for jumping on water is simplified and easily simulated. Table S6 lists the stiffness values of the water surface measured in experiments.

3. Dynamic Modeling of the Robot

The surface tension force is modeled as a spring-damper system due to the force linearly increasing with the depth of dimple as long as the water surface is not broken (Fig. S10). Therefore, a Lagrange formulation for the differential equations of motion can be derived with the following energy equation:

$$\frac{d}{dt}\left(\frac{\partial L}{\partial \dot{\theta}}\right) - \frac{\partial L}{\partial \theta} = -C_w(\dot{\theta}) \quad (7)$$

where $L = T - V$,

$$T = \sum \frac{1}{2} m_i v_i^2 + \sum \frac{1}{2} I_i w_i^2$$

$$V = \frac{1}{2} k_s^2 + \sum \frac{1}{2} m_i g H_i + \frac{1}{2} k_w h^2$$

where T is the kinetic energy, V is the potential energy, v_i is the velocity of each component, C_w is the damping coefficient, I_i is the second moment of inertia, w_i is the angular velocity of each component, g is the gravitational acceleration, and H_i is the height from the ground level. k_w is the stiffness of the water surface, and h is the sinking depth of the legs. k_w varies depending on the length and shape of the wetted part of the legs. In the previous section, we obtained the stiffness of the water surface with the specimen that has the same leg dimensions (Fig. S13). Therefore, we use 0.375 N/m for k_w , the stiffness of the water surface in the dynamic modeling. The damping coefficient (C_w), 0.01, has been obtained from slope of first derivative of the drag force with respect to the sinking velocity.

4. Results and Data

Table S2 lists values from our experimental results and dynamic modeling. The driving force profile is obtained from dynamic modeling owing to practical difficulties in measuring small forces exerted for short durations (Fig. S4). Dynamic modeling produces velocity profiles that match well to the experimentally obtained profiles of jumping on ground, as shown in Fig. S3. However, experimental results on water (except for Fig. S3D) do not match well with the results obtained from the dynamic model because the water surface was broken, which changed the driving force significantly. Wetted length was measured using a video analysis program at the moment of maximum dimple depth. Maximum driving force per wetted length of robot 4 is just below the maximum surface tension force (2σ), 144 mN/m. Therefore, robot 4 shows similar jumping performance on both water and ground (Fig. S3D).

The initial energy stored in the actuator is transformed into the jumping kinetic energy which is then transformed into the gravitational potential energy as the jumping height increases. However, some portion of the energy is dissipated into the vibration kinetic energy of the legs and the robot body, as well as the water surface energy when jumping on water.

The amount of energy transformation is calculated using our dynamic model at the moment of take-off for robot 4, which satisfies the design criteria, and is listed in Table. S7. When jumping on ground, the kinetic energy stored in the vibrations of the legs and the body is 67.4%, and the kinetic energy for jumping is 29.3%. Note that the body has already gained potential energy of 3.3% at take-off. When jumping on water, the kinetic

energy stored in the vibration is 63.5% and energy stored in the water surface is 2%, and the kinetic energy for jumping is 31.3% with potential energy of 3.3%. Note that less energy is dissipated to vibration energy when jumping on water.

Although the energy lost to friction is not included in our models, the amount of energy lost to friction can be estimated from the discrepancy between the modeling and the experimental results of the take-off velocity on ground (see Table S2). The maximum discrepancy occurred for robot 4, showing less than 3% of the initial stored energy.

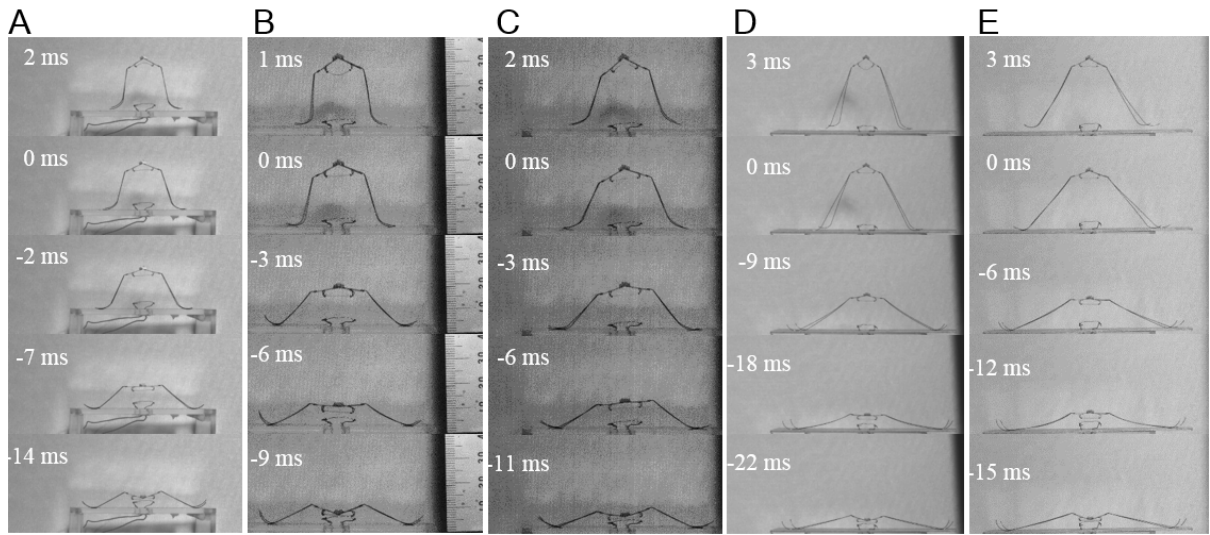


Fig. S1.

Sequential pictures taken by a high-speed camera during take-off on the ground. (A) Robot 1. (B) Robot 2. (C) Robot 3. (D) Robot 4. (E) Robot 5.

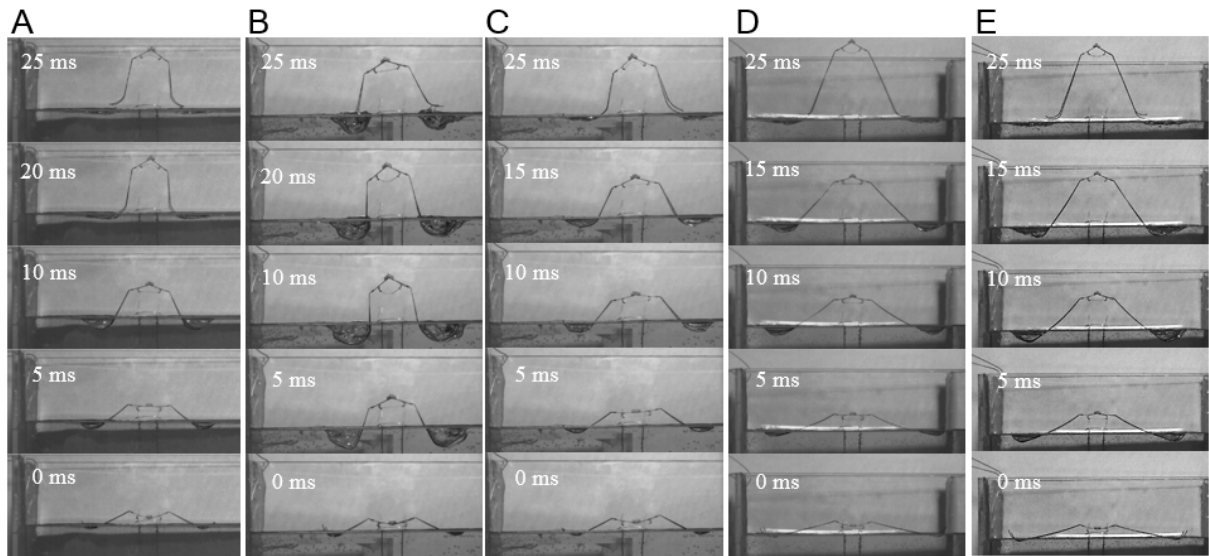


Fig. S2

Sequential pictures taken by a high-speed camera during takeoff on water. (A) Robot 1. (B) Robot 2. (C) Robot 3. (D) Robot 4. (E) Robot 5.

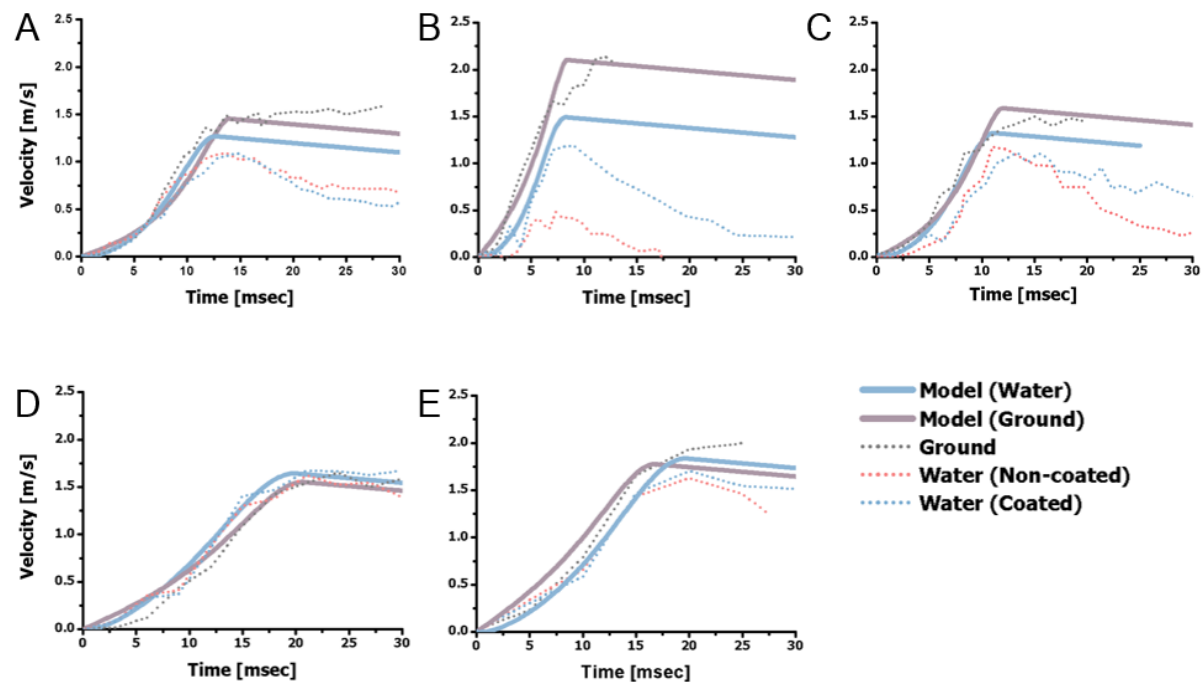


Fig. S3

Velocity of the robot during take-off. The graphs were obtained from experiments and dynamic modeling. (A) Robot 1. (B) Robot 2. (C) Robot 3. (D) Robot 4. (E) Robot 5.

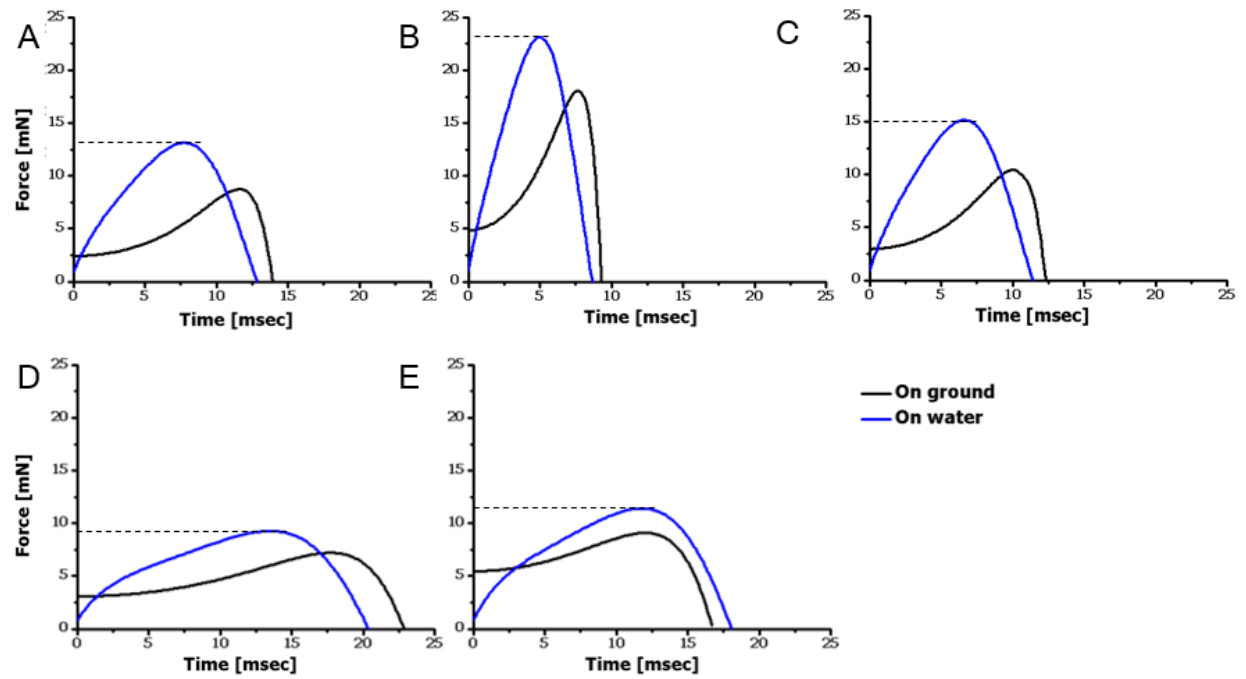


Fig. S4

Driving force profiles obtained by dynamic modeling. (A) Robot 1. (B) Robot 2. (C) Robot 3. (D) Robot 4. (E) Robot 5.

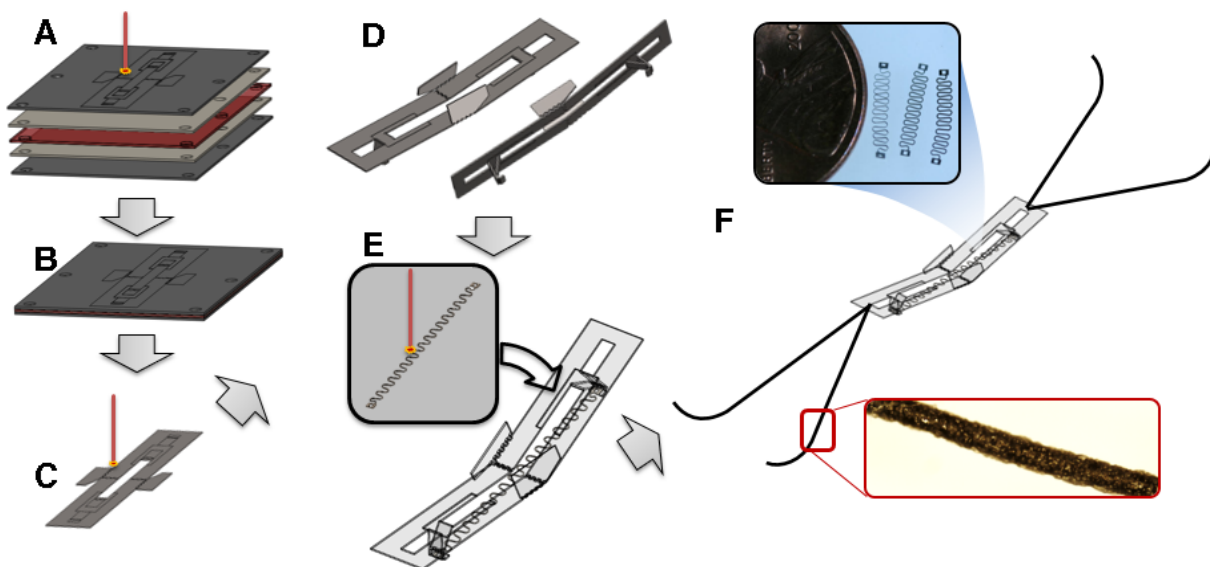


Fig. S5

Fabrication of the jumping robotic insect using SCM (18, 20, 22). (A) Ultraviolet (UV) laser machining of each layer (fiber-reinforced polymers [FRP]-adhesives-polyimide film-adhesives-FRP). (B) Laminating with a heat press. (C) Final cut by UV laser machining to release the functional components. (D) Assembly by folding and locking. (E) Attaching the sheet SMA actuator using SMP blind riveting (29). (F) Attaching legs made of superelastic SMA wire coated with superhydrophobic materials.

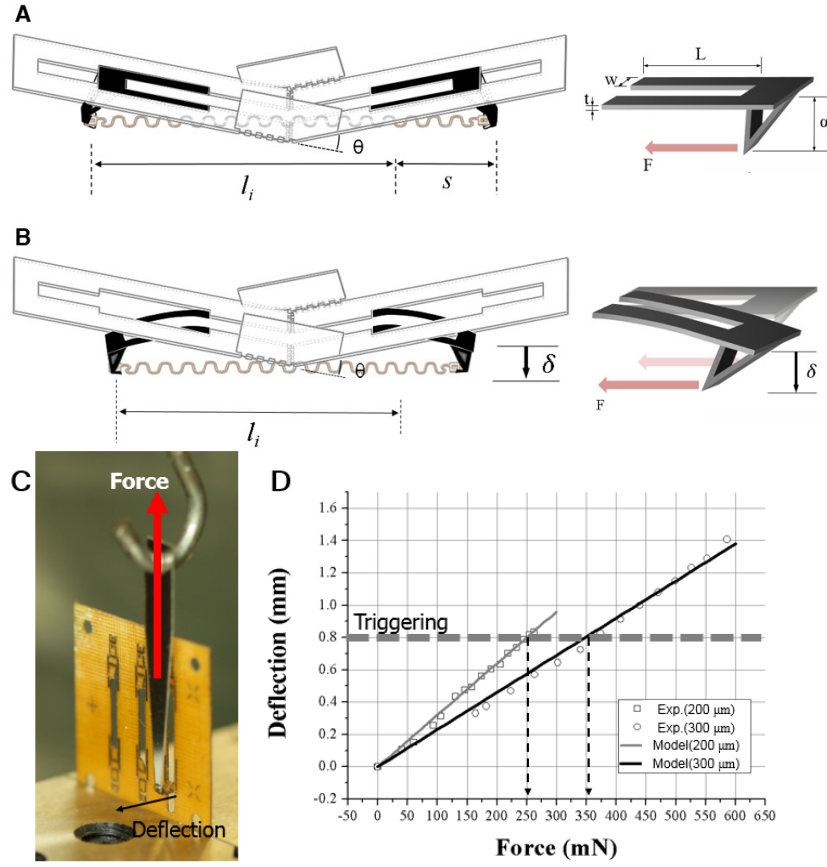


Fig. S6

Illustration of the passive trigger component parameters. (A) Before actuation. (B) The moment of triggering. (C) Experimental setup. (D) Experimental data and modeling results with various widths (w).

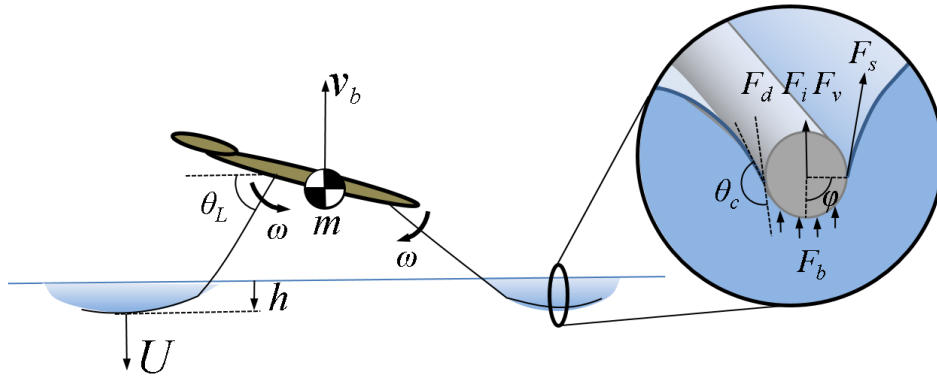


Fig. S7

Illustration of the hydrodynamic forces exerted on the leg of the water strider and robotic water strider at the water surface.

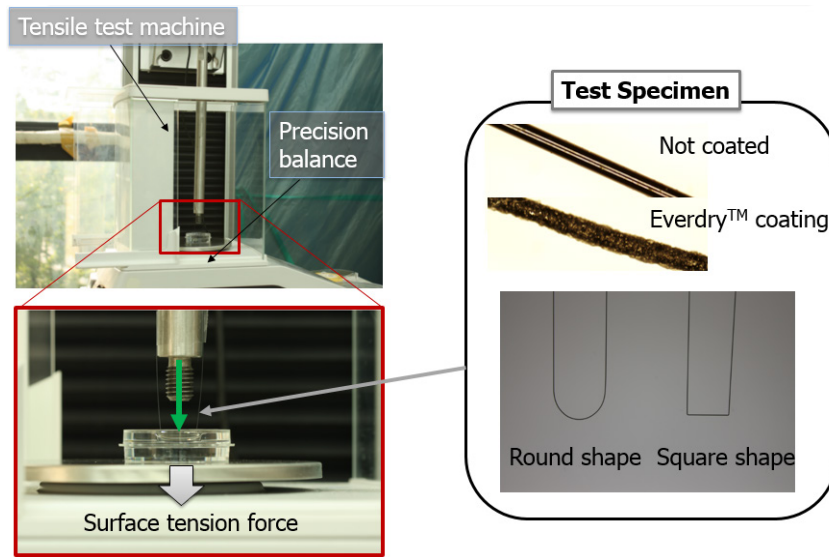


Fig. S8

Experimental setup for measuring the surface tension force at the leg tip.

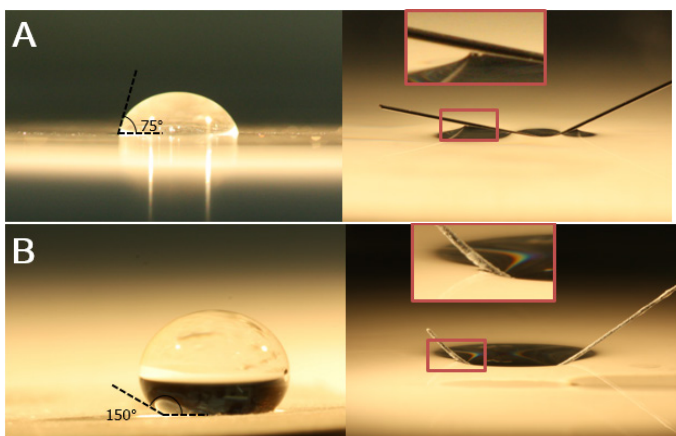


Fig. S9

(A) Uncoated SMA (left: Nitinol sheet, right: Nitinol wire). (B) SMA (Nitinol) coated with hydrophobic material (EverDry™, UltraTech International Inc., left: Nitinol sheet, right: Nitinol wire).

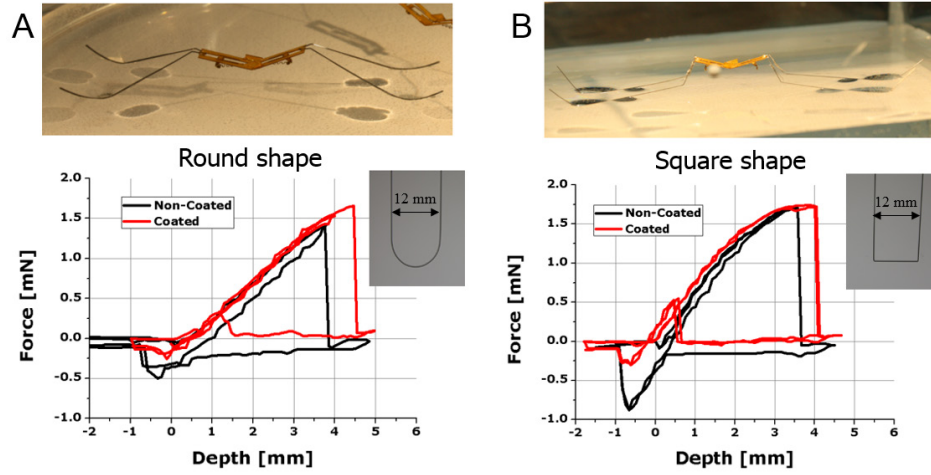


Fig. S10

Measurement results of measuring the stiffness of the water surface. (A) Round shape leg. (B) Square shape leg.

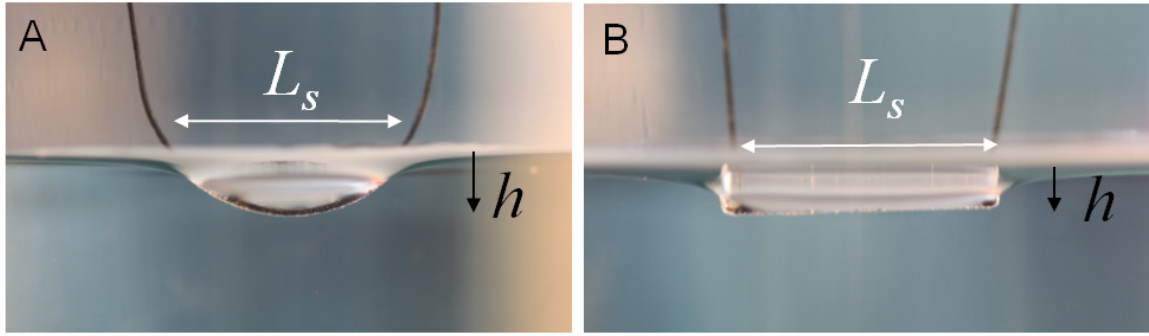


Fig. S11

Side view of experimental measurement of the surface tension force. (A) Round-shaped leg. (B) Square-shaped leg.

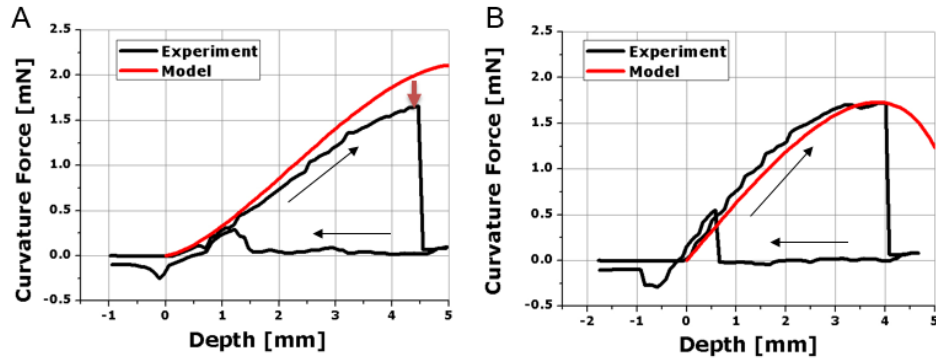


Fig. S12

Analytical modeling and experimental measurement of the surface tension force of the round-shaped leg (A) and the square-shaped leg (B).

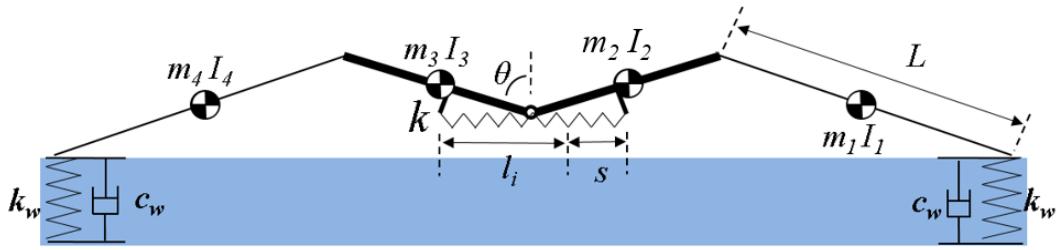


Fig. S13

Dynamic model of the robotic water strider jumping on water.

	Water strider 1	Water strider 2	Water strider 3	Water strider 4
Symbol in Fig. 2	□	■	○	●
Sex	Male	Male	Female	Female
Body mass [mg]	38.4	37.2	49.0	49.0
Wetted length [mm]	46.4	43.6	44.6	44.6
Maximum dimple depth [mm]	2.49	2.88	2.97	2.98
Maximum force [mN]	5.61	5.83	6.07	6.08
Maximum force per unit length [mN/m]	121	133	136	136
Velocity at maximum depth [m/s]	0.92	0.95	0.89	0.69
Take-off velocity [m/s]	1.17	1.30	1.22	0.98
Take-off velocity / Velocity at maximum depth	1.27	1.37	1.37	1.42
Water surface	Not broken	Not broken	Not broken	Not broken

Table S1.
Kinematic parameters of water strider subjects

	Robot 1	Robot 2	Robot 3	Robot 4	Robot 5
Max. driving force on the ground (modeling) [mN]	8.74	18	10.49	7.2	9.09
Max. driving force on water (modeling) [mN]	13.13	23.12	15.15	9.27	11.42
Wetted length [mm]	48	48	48	66	66
Max. driving force (f) / wetted length (l) [mN/m]	273	481	315	140	173
Take-off velocity on the ground (experiment) [m/s]	1.45	2.1	1.48	1.53	2
Take-off velocity on the ground (modeling) [m/s]	1.45	2.11	1.6	1.62	1.9
Take-off velocity on water (experiment) [m/s]	0.6	0.25	0.6	1.67	1.4
Take-off velocity on water (modeling) [m/s]	1.26	1.5	1.4	1.67	1.9
Water-ground velocity ratio (ε_w)	0.41	0.11	0.4	1.09	0.7
Jumping height on ground (experiment) [mm]	107	225	111	119	204
Jumping height on ground (modeling) [mm]	107	227	131	134	184
Jumping height on water (experiment) [mm]	18	3	18	142	100
Jumping height on water (modeling) [mm]	81	114	100	142	184
Water surface	Broken	Broken	Broken	Not broken	Broken

Table S2.

Experimental and dynamic modeling results

	Robot 1	Robot 2	Robot 3	Robot 4	Robot 5
Body mass [mg]	53	64	53	68	68
Leg length [cm]	3			5	
Leg width [mm]	0.2				
Triggering force [mN]	95	201	118	95	118
Actuator stroke [mm]	5.75		4.5	5.75	
Actuator stiffness [N/m]	16.52	35	26	16.52	20.5
Initial angle of the body [°]	32				
Width of passive trigger cantilever [μm]	200		250	200	250
Composite thickness [μm]	170	240	170		

Table S3.
Specifications of the robotic water strider prototypes

Parameter	Description	Characteristic value
C_d	Drag coefficient of the leg	2 at $Re \sim 10^{-10} - 10^2$
ρ	Density of water	10^3 kg/m^3
σ	Coefficient of surface tension of water	0.072 N/m
ν	Coefficient of kinematic viscosity of water	$10^{-6} \text{ m}^2/\text{s}$
g	Gravitational acceleration	9.8 m/s^2
U	Mean velocity of the leg	0.16 m/s (real) 0.24 m/s (robot)
l	Wetted length of leg	10 mm (real) 20 mm (robot)
P	Leg contact perimeter of four legs	80 mm (real) 160 mm (robot)
R	Radius of leg	0.05 mm (real) 0.1 mm (robot)
D	Diameter of leg	0.1 mm (real) 0.2 mm (robot)
M	Mass	40 mg (real) 68 mg (robot)

Table S4.

Characteristic parameters for biological and robotic water strider locomotion

Parameter	Water strider	Robot
$Re = UD/\nu$	16	48
$Bo = \rho g R^2 / \sigma$	3×10^{-4}	1×10^{-3}
$We = \rho U^2 D / \sigma$	0.036	0.165
$Ba = Mg / \sigma P$	0.07	0.06

Table S5.

Dimensionless parameters for real and robotic water strider locomotion

Parameters		Round shape	Square shape
Stiffness of the water surface	Not coated	0.375 N/m	Nonlinear
	Coated	0.375 N/m	Nonlinear
Maximum surface tension force	Not coated	0.057 N/m	0.08 N/m
	Coated	0.07 N/m	0.08 N/m

Table S6.

Stiffness of the water surface obtained from the surface tension force measurement

Energy	On ground	On water
<i>Initial energy in the actuator</i>	0.304 mJ (100%)	0.304 mJ (100%)
<i>Jumping kinetic energy</i>	0.089 mJ (29.3 %)	0.095 mJ (31.3 %)
<i>Vibration kinetic energy</i>	0.205 mJ (67.4 %)	0.193 mJ (63.5 %)
<i>Potential energy</i>	0.010 mJ (3.3 %)	0.010 mJ (3.3 %)
<i>Water surface energy</i>	0.000 mJ (0 %)	0.006 mJ (2.0 %)

Table S7.

Transformation of the initial energy to various energies at the moment of take-off for robot 4 (in modeling)

Movie S1

Movie clip of the robotic insect performing a smooth jump on the water surface without making a large splash. The movie plays at 0.005X real-time speed and was taken with a high-speed camera recording at 3000 frames per second. The robot is prototype number 4, which satisfies the design criteria described in the paper.

Movie S2

Movie clip of a horizontal view of movie S1. The movie plays at 0.005X real-time speed and was taken with a high-speed camera recording at 3000 frames per second. Distortion of the water surface is shown, and the water surface supports the driving force of the legs successfully without breaking.

Movie S3

Movie clip of the robotic insect jumping on the rigid ground. The movie plays at 0.005X real-time speed and was taken with a high-speed camera recording at 3000 frames per second.

Movie S4

Movie clip showing robot prototype 4 jumping on water and on ground. The jumping heights in the two experiments are almost similar. The movie shows that the robot obtains almost the same momentum on water as on rigid ground. The movie plays at 1/8X real-time speed and was taken with a high-speed camera at 240 frames per second.

Movie S5

Movie clip showing water strider jumping on water in front view. The movie plays at 0.03X real-time speed. The water strider was placed in a square acrylic bath (70 mm wide) half-filled with water, and jumping behaviors were recorded from front view using a high-speed camera (TS 1000ME) at 1000 frames per second.